AMERICAN SCIENTIFIC PUBLISHERS

Science of Advanced Materials
Vol. 7, pp. 1–9, 2015
www.aspbs.com/sam

ARTICLE

Nickel-Doped Lithium Trivanadate Nanosheets Synthesized by Hydrothermal Synthesis as High Performance Cathode Materials for Lithium Ion Batteries

Yaguang Liu[1], Huanqiao Song[1], Cuiping Zhang[1], Xihui Nan[1], Chaofeng Liu[1], and Guozhong Cao[1,2,*]

[1]*Beijing Institute of Nanoenergy and Nanosystems, Chinese Academy of Sciences, Beijing 100083, China*
[2]*Department of Materials and Engineering, University of Washington, Seattle, WA 98195-2120, USA*

ABSTRACT

Nickel-doped lithium trivanadate (Ni-LiV_3O_8) with nanosheet structure was synthesized by hydrothermal method. When used as a cathode material, the hydrothermal Ni-LiV_3O_8 exhibited significantly better cycling performance with a capacity of 161.1 mA h g^{-1} after 100 cycles at a 1 C rate (1 C = 300 mA g^{-1}), and much better rate performance compared with sol–gel-derived Ni-LiV_3O_8. The Ni-LiV_3O_8 synthesized by the hydrothermal method contained a large amount of mesopores and consisted of appreciable oxygen vacancies and tetravalent vanadium ions, which make it a competitive candidate for lithium ion batteries with high capacity at moderate discharge voltage.

KEYWORDS: Ni-Doped LiV_3O_8 Nanosheets, Hydrothermal Growth Method, Large Specific Surface Area, Cathode Material for Lithium Ion Batteries, Excellent Rate Performance.

1. INTRODUCTION

Lithium ion batteries (LIBs), being regarded as the predominant power source for portable consumer electronics, have become the most promising in the fields of electric vehicles (EVs) and hybrid electric vehicles (HEVs) because of their high power output and long cycle life.[1–5] However, the rapid advancement of portable electronics and EVs imposes great challenges for the next generation of batteries to fulfill various requirements. For powering electric vehicles, the batteries need to have high gravimetric and volumetric energy densities, so both high discharge voltage and large storage capacity are the critical properties required. Safety and low cost are also equally important. For other applications, high power density is more important leading to rising enthusiasm in the research of hybrid battery supercapacitors.[6] However, some applications demand high energy density with moderate discharge voltage, such as for powering biomedical devices and instruments.[7,8] LiV_3O_8 (henceforth denoted as LVO) has a layer crystal structure that permits lithium ions to insert between adjacent layers, offering a large storage capacity at moderate discharge voltage. LVO thus is an important cathode material for LIBs.[9] However, its poor kinetics, such as low electronic conductivity and lithium ion diffusion coefficient, hinder its practical applications.[10–12]

It is well known that the lithium ion diffusion capability relates to the lithium ion diffusion coefficient and the length of the lithium ion diffusion path.[13–16] Tailoring the nano-scale structure of lithium ion intercalation materials is a feasible and effective way to improve the lithium ion diffusion capability.[17–19] Materials with nano-scale structure possess a large specific surface area to provide more active sites for lithium ion intercalation and can effectively shorten the diffusion length of the lithium ions in the process of the insertion/extraction, thus improving cycling performance and rate capability.[20]

The electrochemical properties of a practical cathode material are strongly dependent on the particle morphology formed under different synthesis methods. It has been demonstrated that engineering the morphology of LVO into one-dimensional and two-dimensional nanostructures (e.g., nanorods[21] and nanosheets[22]) facilitates the electron transport and lithium ion insertion/extraction. High-temperature, solid-state sintering has been used extensively as reported in literature[23] to prepare the $Li_{1+x}V_3O_8$ electrode. The disadvantages of this method, such as particle growth and agglomeration, are obvious, thus several methods have been developed to synthesize nanostructured LVO with controlled morphology

*Author to whom correspondence should be addressed.
Email: gzcao@u.washington.edu
Received: xx Xxxx xxxx
Accepted: xx Xxxx xxxx

ARTICLE

and improved lithium ion storage properties. These effective methods include sol–gel processing,[24–26] hydrothermal growth,[27,28] freeze drying,[29,30] spray drying,[31,32] and microwave synthesis.[33–35] The electrochemical properties and nanostructures of LVO are strongly dependent on the processing methods and parameters. In addition, the capacity fading of LVO is widely observed and attributed to the damage of the crystal structure, which originated from the volume change and the partial dissolution of electrode materials into the electrolyte during cycling.[36] Surface coating and passivation have been explored to improve the structural and chemical stability of LVO subjected to lithium ion intercalation and extraction.[37–39] In addition, metal element doping of the electrode crystal lattice could also improve its electrochemical performance effectively. For example, copper-doped V_2O_5-based cathode has excellent reversibility upon cycling with no capacity fading after 450 cycles.[40]

The present study compares hydrothermal growth and sol–gel processing of Ni-LiV_3O_8 followed by thermal annealing. The formation processes, the morphologies and lithium ion intercalation properties of the resulting Ni-LiV_3O_8 have been investigated and the influences of the synthesis methods, processing parameters and electrochemical properties have been discussed. The experimental results revealed that the hydrothermal method resulted in the formation of mesopores in Ni-LiV_3O_8 nanosheets, which exhibited improved electrochemical properties compared to sol–gel processing.

2. EXPERIMENTAL SECTION

2.1. Material Synthesis

All chemicals used in this work were analytical grade and were used without further purification. The synthesis of Ni-LVO nanosheets was carried out following a procedure reported previously with some modifications.[21] V_2O_5, $CH_3COOLi \cdot 2H_2O$, $(CH_3COO)_2Ni \cdot 4H_2O$ and oxalic acid ($H_2C_2O_4 \cdot 2H_2O$) were used as raw materials to prepare the precursor solution, oxalic acid acted as both a chelating and reducing agent. First, V_2O_5 and oxalic acid in a stoichiometric ratio of 1:3 were dissolved in actively stirred deionized water at room temperature until the color of solution turned from yellow to blue, which indicates that the valance state of V transformed from +5 to +4 and that vandyl oxalate hydrate ($VOC_2O_4 \cdot nH_2O$) formed.[41] This reaction can be expressed as:[22]

$$V_2O_5 + 3H_2C_2O_4 \rightarrow 2VOC_2O_4 + 3H_2O + 2CO_2 \quad (1)$$

Second, a certain amount of $(CH_3COO)_2Ni \cdot 4H_2O$ where Ni accounts for 2% of V was added into the solution and the mixture was stirred for one hour. The color of the liquid turned dark green. A stoichiometric amount of $CH_3COOLi \cdot 2H_2O$ was added and the mixture was vigorously stirred for one hour. Then, the precursor solution was transferred into a Teflon lined stainless steel autoclave and heated at 180 °C for 24 hours. Finally, the mixture was dried overnight in an oven at 80 °C to get the hydrothermal growth powder. At the same time, the other precursor solution was dried overnight in an oven at 80 °C to obtain the sol–gel processing powder.

The as-obtained powders were then annealed at 250, 320 and 400 °C in air for one hour at a temperature ramping rate of 2 °C min^{-1} to get Hydro-Ni-LVO-250, Hydro-Ni-LVO-320, Hydro-Ni-LVO-400, Sol-Ni-LVO-250, Sol-Ni-LVO-320 and Sol-Ni-LVO-400, respectively. As a control, LiV_3O_8 without Ni (denoted as pure LVO) was also prepared using the hydrothermal growth method and annealed at 320 °C for one hour.

2.2. Material Characterization

Differential thermal analysis of samples were carried out using a Mettler Toledo TGA/DSC STAR^e system. X-ray diffraction (XRD) analyses of the samples were conducted on a Marcogroup diffractometer (MXP21 VAHF) with a Cu-Kα radiation source ($\lambda = 1.54056$ Å). Raman spectra were collected at ± 0.65 cm^{-1} resolution with a Horiba JOBIN YVON Raman system (LabRAM HR Evolution) using an argon ion laser (532 nm) as the excitation source. X-ray photoelectron spectroscopy (XPS) was performed on the Thermo Scientific ESCALab 250Xi using 200 W monochromated Al Kα radiation. The 500 μm X-ray spot was used for XPS analysis. The base pressure in the analysis chamber was about 3×10^{-10} mbar. Typically the hydrocarbon C1*s* line at 284.8 eV from adventitious carbon was used for energy referencing. The microstructures of samples and energy dispersive spectroscopy (EDS) mapping of the as-prepared materials were investigated by HITACHI SU8200 cold field emission scanning electron microscope (SEM) and transmission electron microscopy (TEM) investigations were performed using a FEI Tecnai G2 F20 S-TWIN TMP instrument with an accelerating voltage of 200 kV. The total surface area was determined using nitrogen sorption analyses via surface area and porosity analyzer (Micromeritics ASAP 2020 HD88, USA). For the mesopore surface area, pore volume, and pore diameter, the Barrett-Joyner-Halenda (BJH) method was adopted, whereas the specific surface area and the pore volume of micropores were calculated using *t*-method.

2.3. Electrochemical Characterization

Electrochemical tests were carried out using 2032 coin cells assembled in an argon-filled glove-box in which both the content of oxygen and water were below 0.5 ppm. To prepare working electrodes, a mixture of active material, carbon black and poly-(vinyl difluoride) (PVDF) at a weight ratio of 80:10:10 was pasted on an Al foil. The electrolyte was composed of 1 M $LiPF_6$ dissolved in a mixture of ethylene carbonate/dimethyl carbonate/diethyl carbonate (EC/DMC/DEC, 1:1:1 vol%).

A Celgrade polypropylene was used as the separator. To investigate the electrochemical properties of electrode materials, the half cells were adopted and lithium foil was used as the counter electrode.

Galvanostatic charge–discharge tests of assembled cells were performed on a Land CT2001A system (Wuhan, China) under various current densities. The measured voltage range for half cells was in a voltage window of 2.0–4.0 V (vs. Li/Li^+). Cyclic voltammograms (CVs) were conducted on a Solartron SI 1287 at the scanning rate of 0.1 mV s^{-1}. Electrochemical impedance spectroscopy (EIS) was conducted on a Solartron SI 1260 over the frequency range from 100 kHz to 1 mHz with an amplitude of 10 mV. Before the EIS test, the cells were charged to 2.7 V and then kept at that voltage for a period of time to reach a stable state. All electrochemical measurements were carried out at room temperature. The current densities for the half cells were all determined based on the mass of active materials on electrodes.

3. RESULTS AND DISCUSSION

3.1. Structural Characterization

Figure 1 shows the TG/DTA curves of the Ni-LiV_3O_8 precursor powders synthesized by sol–gel processing (a) and hydrothermal growth (b) under flowing air at a ramping rate of 10 °C min^{-1}. The slow weight-loss between 40 and 250 °C (Fig. 1(a)) resulted from the loss of physically and chemically bound water in the Ni-LiV_3O_8 samples. The significant weight loss between 250 and 320 °C and the corresponding exothermal peak in the DTA curve are attributed to the decomposition of inorganic precursor such as VOC_2O_4, CH_3COOLi and $(CH_3COO)_2Ni$. With increased temperature, a small exothermal peak appears which corresponds to two exothermal reactions, probably resulting from the combustion of a small amount of the residual carbon and the further oxidation of V^{4+} in air.[22] The stable weight suggests that the extra weight gained from oxidation and the mass loss of carbon are both small and almost equal in the process.

Figure 1(b) shows TG/DTA curves of the precursor synthesized through hydrothermal method. No significant difference in TG curves is detected between two samples at temperatures range of 40–250 °C, suggesting a similar water loss process. The larger water loss observed for the hydrothermal method could have resulted from the greater number of steps in the hydrothermal growth procedure compared to the sol–gel process. There is a rapid weight loss for the precursor between 250 and 320 °C, which also can be attributed to the decomposition of inorganic precursor. The gradual weight increase occurs between 320 and 600 °C derived from further oxidation of V^{4+} in air.

Figure 2(a) shows the XRD patterns of the samples Sol-Ni-LVO-320, Hydro-Ni-LVO-320, Sol-Ni-LVO-400, Hydro-Ni-LVO-400 and pure LVO, respectively. There are no remarkable differences in peak positions

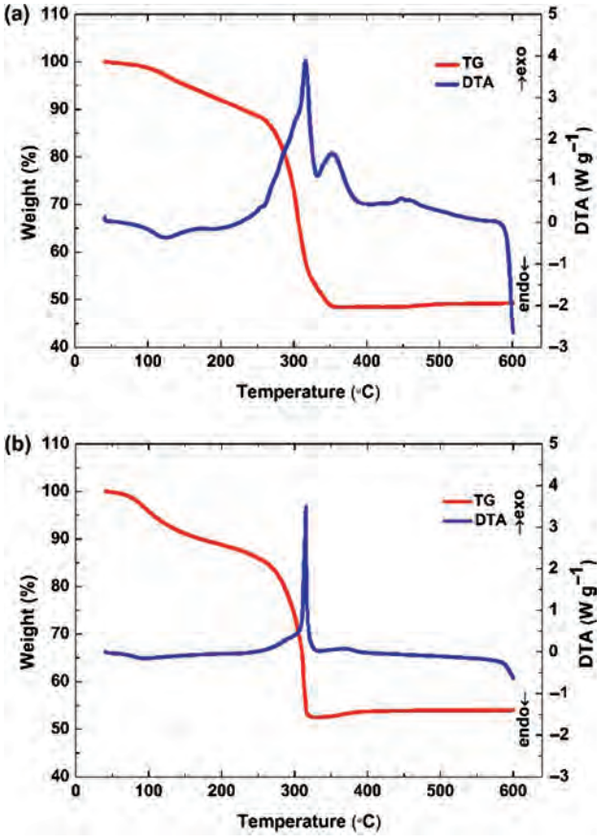

Fig. 1. TG and DTA curves for the Ni-LiV_3O_8 precursor powders synthesized by sol–gel processing (a) and hydrothermal growth (b) methods.

of all samples either synthesized by sol–gel processing or hydrothermal growth. All patterns show the samples contained neither nickel metal nor $(CH_3COO)_2Ni$, as Ni is most likely to be incorporated to the LVO compound by substituting with vanadium ion positions as this work intended to accomplish. Such substitution has been done in vanadium pentoxide.[42] In addition, the peak intensity, which indicates the high crystallinity of LVO, increases with annealing temperature. The XRD peak positions for all samples are in agreement with the layered-type LiV_3O_8 (JCPDS 72-1193).[43,44] For all samples, a $Li_{0.3}V_2O_5$ impurity phase exists, which has also been previously observed in LVO produced by other methods.[34,45] Figure 2(b) shows the XRD patterns of the samples synthesized by sol–gel and hydrothermal method and annealed at 250 °C. The XRD peak positions for the samples indicate they are both LiV_2O_5 (JCPDS 18-0756).[46] However, the XRD pattern does not show any obvious change in lattice parameter between nickel doped LVO and pure LVO. The Raman spectra of doped and undoped samples were compared in order to verify whether or not the LVO powders were successfully doped with nickel ions. Figure 2(c) shows the Raman spectra of the pure LVO, Sol-Ni-LVO-320 and Hydro-Ni-LVO-320. The Raman band of pure LVO

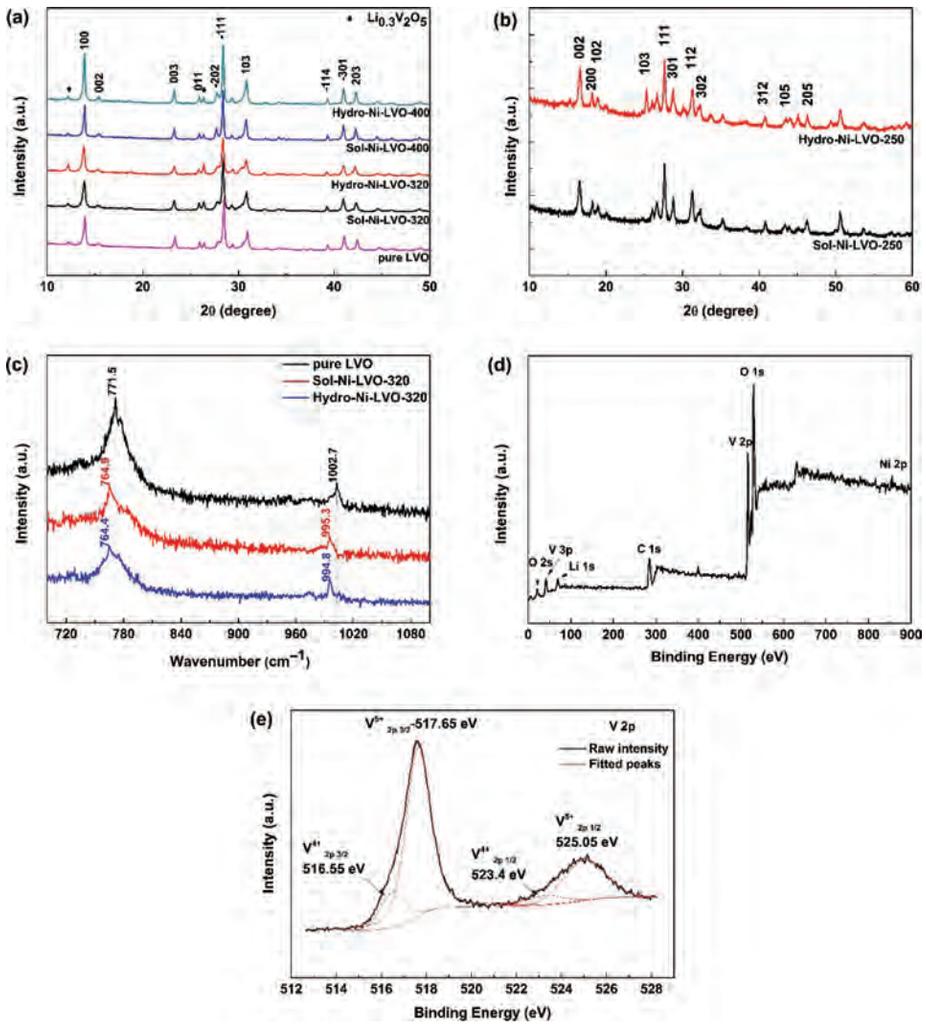

Fig. 2. (a) XRD patterns of pure LVO, Sol-Ni-LVO-320, Hydro-Ni-LVO-320, Sol-Ni-LVO-400 and Hydro-Ni-LVO-400; (b) XRD patterns of Sol-Ni-250 and Hydro-Ni-250; (c) Raman spectra of pure LVO, Sol-Ni-LVO-320 and Hydro-Ni-LVO-320; XPS spectra of Hydro-Ni-LVO-320: (d) survey spectrum and (e) high-resolution V 2*p* spectra.

at 1002.7 cm^{-1} is attributed to the vibrational modes belonging to the A_g symmetry, and can be assigned to V–O stretching vibrations of the VO_5 pyramids.[47] The band at 771.5 cm^{-1} is due to the atomic motions of corner-sharing oxygen among the VO_6, VO_5 and LiO_6 polyhedron.[22,47] The symmetry stretching modes shift to lower wave numbers both in Sol-Ni-LVO-320 (995.3 cm^{-1}, 764.9 cm^{-1}) and Hydro-Ni-LVO-320 (994.8 cm^{-1}, 764.4 cm^{-1}) because the mass of Ni (58.70) is greater than that of V (50.94). The mode shifts indicate a little distortion of the crystal cells, which suggests that Ni substitutes V in the VO_6 octahedron and VO_5 trigonal bi-pyramids.[48]

XPS survey spectrum of Hydro-Ni-LVO-320 (Fig. 2(d)) shows the peaks of Li 1*s*, V 2*p*, and O1*s* clearly but the peak of Ni 2*p* is not obvious due to its small quantity. Figure 2(e) is the high resolution XPS of V 2*p* after fitting in which two main peaks at 517.65 eV and 525.05 eV could be ascribed to the spin-orbit splitting of the components, V^{5+} 2*p*3/2 and V^{5+} 2*p*1/2.[49] It is noteworthy that the peaks of V^{4+} are also clearly found at 516.55 eV (V^{4+} 2*p*3/2) and 523.4 eV (V^{4+} 2*p*1/2),[50] suggesting the existence of V^{4+} in Hydro-Ni-LVO-320 as is reflected in the TG curve (shown in Fig. 1(b)). The relative atomic ratio of V^{5+} and V^{4+} is calculated based on the fitted peak areas, and the value is 5.3:1. A small amount of V^{4+} have shown to benefit the lithium ion intercalation as it generates oxygen vacancies and introduce electron hoping conduction. A large fraction of tetravalent vanadium ions would change the crystal structure and consequently the lithium ion intercalation properties. When the vanadium oxide sample is heated to a high temperature in air, some pentavalent ions convert to tetravalent ions, at the same time oxygen vacancies are generated to maintain the electroneutrality. The presence of both tetravalent vanadium ions and oxygen vacancies in various vanadium oxide compounds has been reported in literature.[51]

Based on these special effects, the defects play an essential role in improving the electrical/ionic conductivity of electrode.[52]

Figure 3 compares the morphologies of the Ni-LiV_3O_8 materials synthesized using the sol–gel method and hydrothermal method and annealed at 320 and 400 °C. The particles are nano-sized in the Ni-LiV_3O_8 synthesized using both methods at 320 °C. The SEM image of Ni-LiV_3O_8 produced by the sol–gel method and annealed at 320 °C (Fig. 3(a)) exhibits that the particles have uniform morphology with aggregation. The sheets are 200–300 nm long, 50–100 nm wide and ~20 nm thick. Ni-LiV_3O_8 nanosheets synthesized by hydrothermal growth (Fig. 3(b)) have a smaller size, with 100–200 nm length, ~50 nm width and ~20 nm thickness. The EDS dot-mapping images of Hydro-Ni-LVO-320 (Figs. 4(b)–(f)) also reveal the uniform distribution of all the elements Li, V, Ni and O. Combining the elements mapping and Raman results, we can conclude that Ni uniformly substitutes in the crystal lattice of LVO. As shown in Figures 3(c)–(d), the nanosheets annealed at 400 °C for one hour in air have a larger size and less space than the samples annealed at 320 °C. As shown in Figure 4(a), the particle of pure LVO has nanosheet morphology with a sheet size of 200–300 nm long, 100–200 nm wide and ~20 nm thick.

Figure 5 shows the TEM image of Sol-Ni-LVO-320 and Hydro-Ni-LVO-320. As shown in Figure 5(a), Sol-Ni-LVO-320 shows nanosheet morphology. In comparison, there are numerous mesopores in the nanosheets of Hydro-Ni-LVO-320 (Fig. 5(b)) which increase its specific surface area and facilitate the diffusion of ions. The inset HR-TEM image shows the lattice space is 0.215 nm which corresponds to (301) of LVO.

The specific surface areas of Sol-Ni-LVO-320, Hydro-Ni-LVO-320 and pure LVO measured by means of nitrogen sorption isotherms as shown in Figure 6 are 25.4, 34.8 and 16.4 $m^2\ g^{-1}$, respectively. The pore volume of micropores of the three samples is also determined from the same nitrogen sorption isotherms and found to be 0.126, 0.283 and 0.0979 $cm^3\ g^{-1}$. This nitrogen sorption results coincide to the analysis of TEM/SEM images.

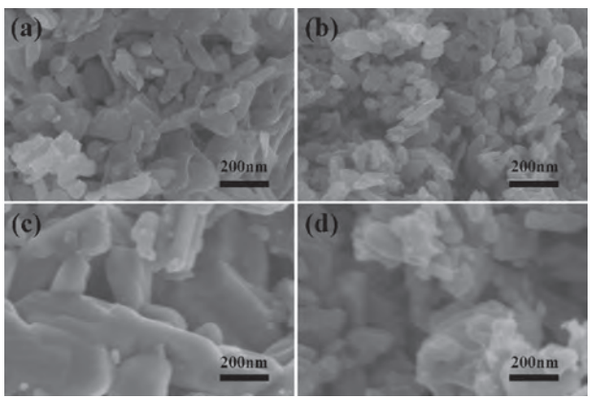

Fig. 3. SEM images of the Ni-LiV_3O_8 synthesized by sol–gel processing and hydrothermal growth methods and annealed at 320 and 400 °C, respectively. (a) Sol-Ni-LVO-320, (b) Hydro-Ni-LVO-320, (c) Sol-Ni-LVO-400, and (d) Hydro-Ni-LVO-400.

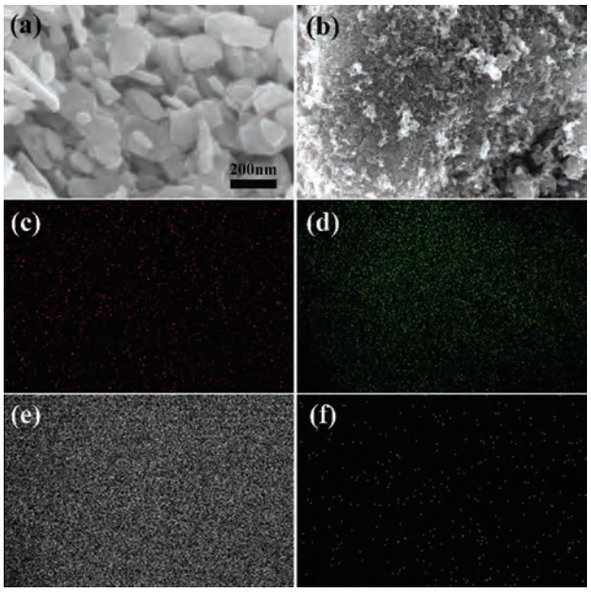

Fig. 4. (a) SEM image of pure LVO; (b) SEM image of Hydro-Ni-320 and EDS dot-mapping images of Li (c), O (d), V (e) and Ni (f) of Hydro-Ni-LVO-320.

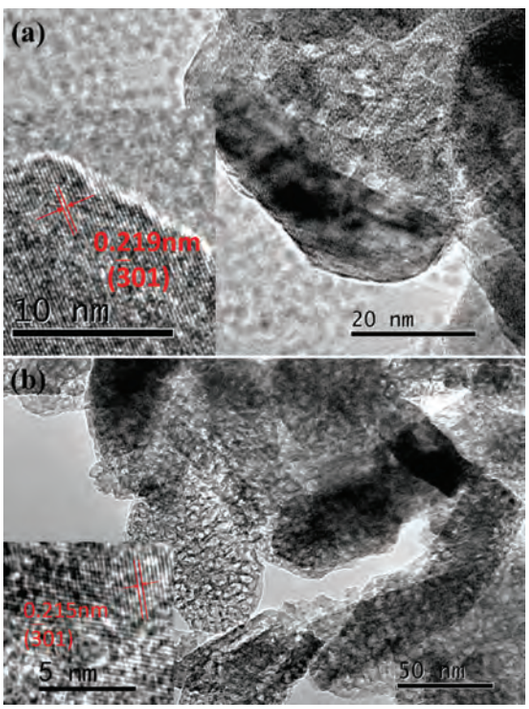

Fig. 5. TEM image of Sol-Ni-LVO-320 (a) and Hydro-Ni-LVO-320 (b).

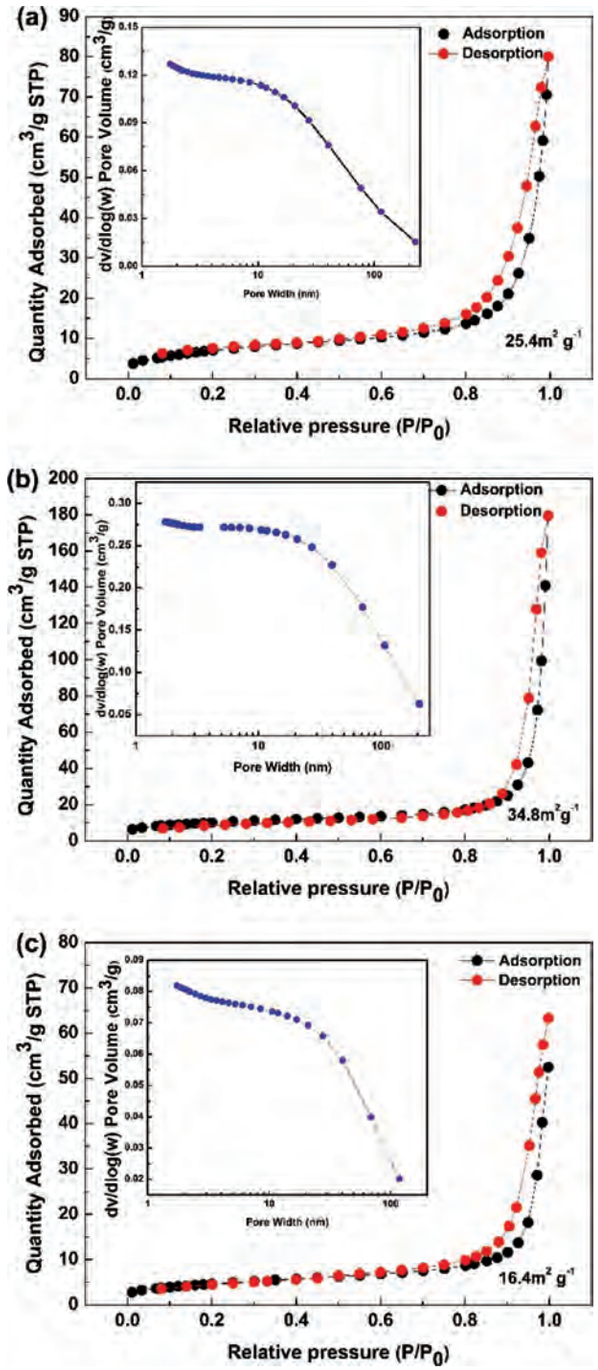

Fig. 6. The specific surface area and the corresponding BJH pore-size distribution curve (inset) Sol-Ni-LVO-320 (a), Hydro-Ni-LVO-320 (b) and pure LVO (c).

3.2. Electrochemical Performance

Figure 7(a) shows the second CV curves of the pure LVO, Sol-Ni-LVO-320 and Hydro-Ni-LVO-320 electrodes at a scan rate of 0.1 mV s^{-1} between 2.0 V and 4.0 V versus Li/Li^+. During the cathodic scan of pure LVO, the peak at ~3.60 V is related to the initial lithium ion inserted into the octahedral site of the LVO host structure.[53] The peak at ~2.76 V belongs to the lithium ion insertion in the empty tetrahedral site by a single-phase reaction between $0 < x < 2.0$ in $Li_{1+x}V_3O_8$, and the peak at ~2.51 V corresponds to the lithium ion occupied tetrahedral sites with a two-phase reaction from $Li_3V_3O_8$ to $Li_4V_3O_8$ ($2.0 < x < 3.0$).[54–56] The corresponding anodic peaks for pure LVO at ~3.67 V, ~2.96 V and ~2.49 V are the lithium ions extraction reaction. Meanwhile one small peak at 3.49 V in the anodic scan and two peaks at 3.15 V and 3.41 V in the cathodic scan correspond to lithiation/delithiation reactions of the active phase of $Li_{0.3}V_2O_5$ as observed in the XRD results of pure LVO, indicating the different lithium ion sites with energy difference for lithium ion holding.[57,58] As for the Sol-Ni-LVO-320 electrode, three peaks at 3.57 V, 3.40 V and 2.32 V are observed during the cathodic scan and three peaks at 3.67 V, 3.22 V and 2.49 V during the anodic scan. The large potential intervals of the Sol-Ni-LVO-320 electrode between the cathodic and anodic peaks reflect the poorly reversible reaction of lithium ions. However, the main cathodic peaks of the Hydro-Ni-LVO-320 electrode shift to ~3.60 V, ~2.76 V and ~2.52 V compared to ~3.60 V, ~2.76 V and 2.51 V of the pure LVO electrode. Likewise, the main anodic peaks shift to ~3.73 V, ~2.94 V and ~2.48 V from ~3.67 V, ~2.96 V and ~2.49 V of the pure LVO electrode. The amount of nickel incorporated into LVO is rather small, thus it is reasonable to see an absence of redox peaks or significant shift in redox peaks of vanadium ions. The presence of Ni in the LVO lattice played a significant role in defining particle morphology in terms of porosity and surface area. The small potential intervals between the cathodic and anodic peaks of the Hydro-Ni-LVO-320 electrode indicate an excellent reversible insertion/extraction reaction for lithium ions. As shown in Figure 7(b), three CV curves of Hydro-Ni-LVO-320 electrode are almost imposed over each other. The existence of Ni stabilizes LVO crystal structure which benefits the insertion/extraction of lithium ions within the layered LVO structure as reported with the Ce-doped and Si-doped LVO.[59,60] The peak positions shown on the CV curves correspond well with the charge/discharge plateaus (shown in Fig. 7(d)). The peak in the charge process observed at 3.73 V results from extraction of pre-existing lithium of LiV_3O_8, which allows intercalation of more lithium ions during the next cycle. This peak can also explain the charge capacity increase observed from the 1st cycle to the 2nd cycle (shown in Fig. 7(d)).[22]

Figure 7(c) gives the cycling performance of pure LVO, Sol-Ni-LVO-320 and Hydro-Ni-LVO-320 electrodes at a current density of 300 mA g^{-1} between 2.0 V and 4.0 V. The pure LVO electrode delivers an initial discharge capacity of 113.4 mA h g^{-1}, however, it sharply decreases to 52.2 mA h g^{-1} at the 100th cycle. This result is in good agreement with literature[34] which reported a remarkable capacity loss in initial cycles of pure LVO. The capacity fading may be attributed to the irreversible phase transition

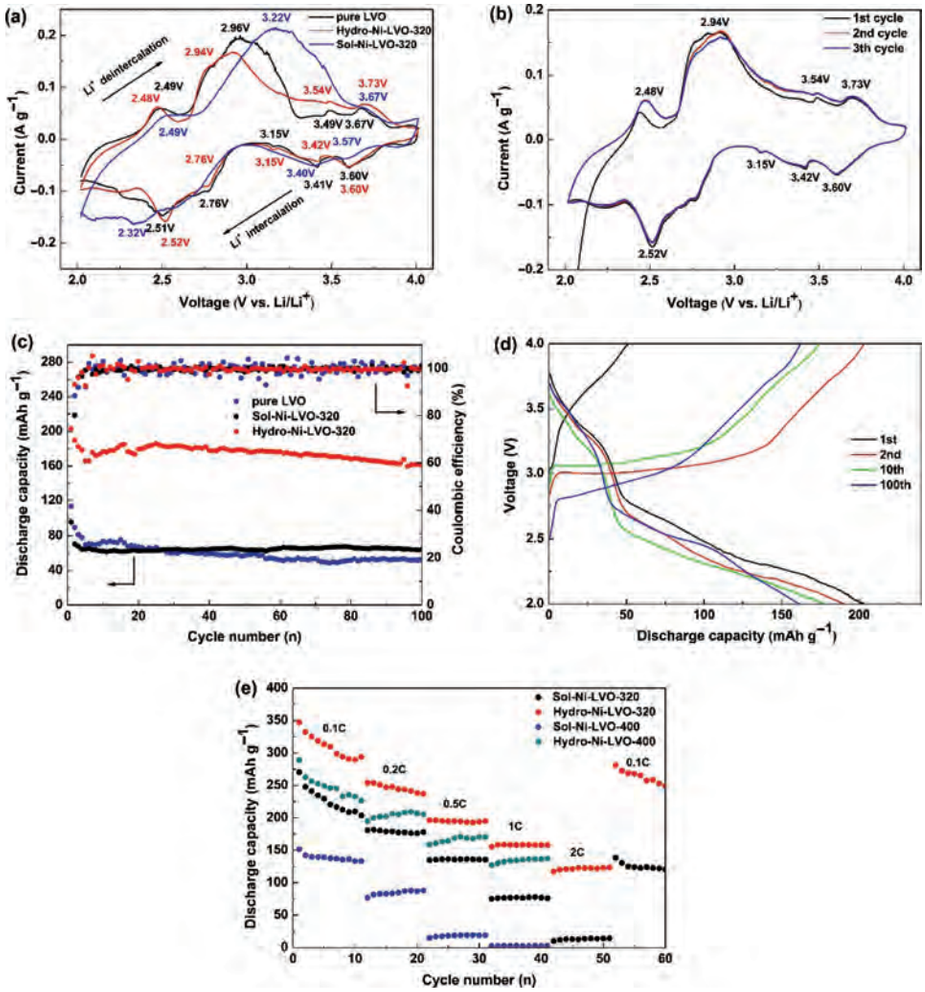

Fig. 7. Electrochemical performance. (a) CV curves of the second cycle of pure LVO, Sol-Ni-LVO-320 and Hydro-Ni-LVO-320 electrodes at a scan rate of 0.1 mV s^{-1} between 2.0 V and 4.0 V versus Li/Li^+; (b) three CV curves of Hydro-Ni-LVO-320 electrode (c) cycling performance of pure LVO, Sol-Ni-LVO-320 and Hydro-Ni-LVO-320 electrodes at a current density of 300 mA g^{-1} between 2.0 V and 4.0 V; (d) charge–discharge curves of Hydro-Ni-LVO-320 at a current density of 300 mA g^{-1} between 2.0 V and 4.0 V at different cycles and (e) rate performance of samples synthesized by sol–gel processing and hydrothermal growth methods and annealed at 320 and 400 °C.

between LiV_3O_8 and $Li_4V_3O_8$,[61] or deterioration of the crystal structure.[36] The Sol-Ni-LVO-320 electrode delivers a discharge capacity of 95.7 mA h g^{-1} at the 1st cycle, but it decreases to 63.9 mA h g^{-1} after 100 cycles. By contrast, Hydro-Ni-LVO-320 electrode shows a higher discharge capacity and better cycling stability. The initial discharge capacity of Hydro-Ni-LVO-320 reaches up to 203.1 mA h g^{-1} and also remains 161.1 mA h g^{-1} after 100 cycles. It shows the highest discharge capacity and lower capacity fading than the pure LVO electrode. Therefore, it suggests that the doping of Ni can stabilize the LVO crystal structure, which decreases the irreversible phase transition between LiV_3O_8 and $Li_4V_3O_8$ during cycles. It is noteworthy that the Sol-Ni-LVO-320 electrode shows good cyclic stability. The reason is likely due to its small capacity causing insignificant variation (expansion and contraction) of the crystal structure during the charge/discharge process, consequently resulting in a good cyclic stability. Moreover, the good cyclic performance of the Hydro-Ni-LVO-320 electrode is attributed to the more active sites and shortened path way for lithium ions. It also can be seen in Figure 7(d) that the capacity fading is not appreciable and obvious plateaus appear in the charge/discharge curves. The small capacity during the 1st cycle (51.0 mA h g^{-1}) could be caused by an incomplete reaction in the cell and insufficient contact between active material and electrolyte.

The superior electrochemical performance of the Hydro-Ni-LVO-320 sample should be attributed to the highly effective space created by the hydrothermal method. As shown in Figure 3, the ample space between sheets can allow sufficient penetration of electrolyte, thus increasing the interfacial area between the electrode and the electrolyte. Jouanneau et al.[62] reported that the particle

size and shape influence the insertion rate of lithium ion which plays a major role in the cyclability. In addition, the size of particles are uniform and small, which would be convenient for the lithium-ion diffusion. Moreover, the nanosheet morphology may be more capable of maintaining the integrity of the structure than other microstructures of LVO electrode materials. When several lithium ions intercalate into the crystal structure of active materials, lattice expansion can potentially breakdown the crystalline structure, resulting in capacity fading over many cycles. However, the nanosheet structure tolerated structural variations during the charge/discharge process, leading to a better cyclic stability.

Figure 7(e) shows the rate performance of four samples synthesized by sol–gel processing and hydrothermal growth methods annealed at 320 and 400 °C in the voltage range between 2.0 V and 4.0 V versus Li/Li$^+$. The current density increased from 0.1 C to 2 C in a stepwise manner and then returned to 0.1 C. Sol-Ni-LVO-320 delivers discharge capacities of 270.5, 181, 134.7, 75.2 and 12.9 mA h g^{-1} at 0.1, 0.2, 0.5, 1 and 2 C, respectively, then 138.4 mA h g^{-1} at 0.1 C, indicating relatively poor rate capability. In comparison, Hydro-Ni-LVO-320 shows the best performance with discharge capacities of 347.1, 254.1, 196.4, 158.4 and 120.2 mA h g^{-1} at 0.1, 0.2, 0.5, 1 and 2 C, respectively, then 281.8 mA h g^{-1} at 0.1 C. Also, the samples annealed at 400 °C show a similar character. It is concluded that the sample produced from the hydrothermal method has a better rate performance than the one by the sol–gel method. Among all four samples, Hydro-Ni-LVO-320 shows the best rate performance.

The EIS results of Sol-Ni-LVO-320 and Hydro-Ni-LVO-320 in the form of Nyquist plots are presented in Figure 8, which shows one depressed semicircle in the medium frequency range. The mediate semicircle is attributed to the charge-transfer resistance (R_{ct}).[63,64] The sloped line represents the Warburg impedance (Z_w) at low frequency, indicating the diffusion of lithium ions in the solid matrix.[63] The fitted results of R_s and R_{ct}

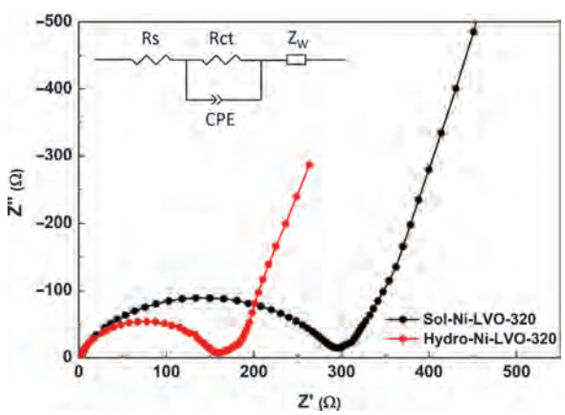

Fig. 8. Nyquist plots of Sol-Ni-LVO-320 and Hydro-Ni-LVO-320 at 2.7 V versus Li/Li$^+$.

Table I. Impedance parameters calculated from equivalent circuit.

Sample ID	R_s (Ω)	R_{ct} (Ω)
Sol-Ni-LVO-320	1	327
Hydro-Ni-LVO-320	0.5	165

of Sol-Ni-LVO-320 and Hydro-Ni-LVO-320 electrode are shown in Table I. Obviously, the R_{ct} of the Hydro-Ni-LVO-320 electrode (165 Ω) is smaller than that of the Sol-Ni-LVO-320 electrode (327 Ω). It is well known that the R_{ct} involves many factors, such as electronic conductivity, crystal structure, the inter-particle contacts and the electrode surface condition.[65] As a result, the suppression of R_{ct} was considered as an important factor for the improvement of the active materials.[66,67] Idris et al.[66] believed that the lower R_{ct} as a reason for better electrochemical performance of carbon coated LVO. Apparently, the sample synthesized through the hydrothermal method suppresses the charge-transfer resistance, thus resulting in superior electrochemical properties.

4. CONCLUSIONS

Ni-LiV_3O_8 nanosheets were successfully synthesized by hydrothermal method. Compared with Ni-LiV_3O_8 synthesized by the sol–gel method, the one synthesized by the hydrothermal method and thermal annealing at 320 °C displayed significantly better cycling performance (80% of initial capacity maintaining after 100 cycles at 1 C) and excellent rate performance. It was evident that the hydrothermal method could not only create more mesopores for the penetration of electrolyte, but also oxygen vacancies which provide more active sites for lithium ions, resulting in a better electrochemical performance. These results suggest that the Ni-LiV_3O_8 synthesized by hydrothermal method is a promising cathode material for lithium ion batteries.

Acknowledgment: This work was supported by the "Thousands Talents" program for a pioneer researcher and his innovative team, China. This work was also supported by the National Science Foundation of China (51374029), Program for New Century Excellent Talents in University (NCET-13-0668), Fundamental Research Funds for the Central Universities (FRF-TP-14-008C1) and China Postdoctoral Science Foundation (2014M550675).

References and Notes

1. M. Armand and J. M. Tarascon, *Nature* 451, 652 (**2008**).
2. X. L. Ji, K. T. Lee, and L. F. Nazar, *Nat. Mater.* 8, 500 (**2009**).
3. B. Kang and G. Ceder, *Nature* 458, 190 (**2009**).
4. J. Maier, *Nat. Mater.* 4, 805 (**2005**).
5. B. Dunn, H. Kamath, and J. M. Tarascon, *Science* 334, 928 (**2011**).
6. D. P. Dubal, O. Ayyad, V. Ruiz, and P. Gomez-Romero, *Chem. Soc. Rev.* (**2015**).

7. J. Qin, W. Lv, Z. Li, B. Li, F. Kang, and Q.-H. Yang, *Chem. Commun.* 50, 13447 (**2014**).
8. C. L. Schmidt and P. M. Skarstad, *J. Power Sources* 97–98, 742 (**2001**).
9. H. L. Zhang, J. R. Neilson, and D. E. Morse, *J. Phys. Chem. C* 114, 19550 (**2010**).
10. Y. Li, Z. Y. Fu, and B. L. Su, *Adv. Funct. Mater.* 22, 4634 (**2012**).
11. L. Q. Mai, X. Xu, L. Xu, C. H. Han, and Y. Z. Luo, *J. Mater. Res.* 26, 2175 (**2011**).
12. M. S. Whittingham, *Dalton T* 5424 (**2008**).
13. J. Jin, S. Z. Huang, J. Liu, Y. Li, D. S. Chen, H. E. Wang, Y. Yu, L. H. Chen, and B. L. Su, *J. Mater. Chem. A* 2, 9699 (**2014**).
14. N. Spinner and W. E. Mustain, *J. Electroanal. Chem.* 711, 8 (**2013**).
15. L. Kavan, J. Rathousky, M. Gratzel, V. Shklover, and A. Zukal, *J. Phys. Chem. B* 104, 12012 (**2000**).
16. B. Varghese, M. V. Reddy, Z. Yanwu, C. S. Lit, T. C. Hoong, G.V. S. Rao, B. V. R. Chowdari, A. T. S. Wee, C. T. Lim, and C. H. Sow, *Chem. Mater.* 20, 3360 (**2008**).
17. W. J. Liu, D. Shao, G. E. Luo, Q. Z. Gao, G. J. Yan, J. R. He, D. Y. Chen, X. Y. Yu, and Y. P. Fang, *Electrochim. Acta* 133, 578 (**2014**).
18. Y. C. K. Chen-Wiegart, R. DeMike, C. Erdonmez, K. Thornton, S. A. Barnett, and J. Wang, *J. Power Sources* 249, 349 (**2014**).
19. H. Guo, R. Mao, X. J. Yang, and J. Chen, *Electrochim. Acta* 74, 271 (**2012**).
20. Y. Wang, Y. Wang, E. Hosono, K. Wang, and H. Zhou, *Angew. Chem. Int. Edit.* 120, 757 (**2008**).
21. A. Q. Pan, J. Liu, J. G. Zhang, G. Z. Cao, W. Xu, Z. M. Nie, X. A. Jie, D. W. Choi, B. W. Arey, C. M. Wang, and S. Q. Liang, *J. Mater. Chem.* 21, 1153 (**2011**).
22. A. Q. Pan, J. G. Zhang, G. Z. Cao, S. Q. Liang, C. M. Wang, Z. M. Nie, B. W. Arey, W. Xu, D. W. Liu, J. Xiao, G. S. Li, and J. Liu, *J. Mater. Chem.* 21, 10077 (**2011**).
23. G. Pistoia, S. Panero, M. Tocci, R. V. Moshtev, and V. Manev, *Solid State Ionics* 13, 311 (**1984**).
24. Y. X. Gu and F. F. Jian, *J. Sol–Gel Sci. Techn.* 46, 161 (**2008**).
25. K. P. Lee, K. M. Manesh, K. S. Kim, and A. Y. Gopalan, *J. Nanosci. Nanotechnol.* 9, 417 (**2009**).
26. L. Liu, L. F. Jiao, Y. H. Zhang, J. L. Sun, L. Yang, Y. L. Miao, H. T. Yuan, and Y. M. Wang, *Mater. Chem. Phys.* 111, 565 (**2008**).
27. X. L. Li, P. P. Li, M. Luo, X. Y. Chen, and J. J. Chen, *J. Solid State Electr.* 14, 1325 (**2010**).
28. H. M. Liu, Y. G. Wang, K. X. Wang, Y. R. Wang, and H. S. Zhou, *J. Power Sources* 192, 668 (**2009**).
29. O. A. Brylev, O. A. Shlyakhtin, A. V. Egorov, and Y. D. Tretyakov, *J. Power Sources* 164, 868 (**2007**).
30. K. West, B. Z. Christiansen, S. Skaarup, Y. Saidi, J. Barker, I. I. Olsen, R. Pynenburg, and R. Koksbang, *J. Electrochem. Soc.* 143, 820 (**1996**).
31. M. Y. Saidi, J. Barker, and E. S. Saidi, *Solid State Ionics* 82, 203 (**1995**).
32. N. Tran, K. G. Bramnik, H. Hibst, J. Prolss, N. Mronga, M. Holzapfel, W. Scheifele, and P. Novak, *J. Electrochem. Soc.* 155, A384 (**2008**).
33. F. Wu, L. Wang, C. Wu, Y. Bai, and F. Wang, *Mater. Chem. Phys.* 115, 707 (**2009**).
34. G. Yang, G. Wang, and W. H. Hou, *J. Phys. Chem. B* 109, 11186 (**2005**).
35. Y. Zhou, H. F. Yue, X. Y. Zhang, and X. Y. Deng, *Solid State Ionics* 179, 1763 (**2008**).
36. S. Jouanneau, A. L. La Salle, A. Verbaere, and D. Guyomard, *J. Electrochem. Soc.* 152, A1660 (**2005**).
37. Q. Qiu, X. Huang, Y. M. Chen, Y. Tan, and W. Z. Lv, *Ceram. Int.* 40, 10511 (**2014**).
38. J. H. Lee, J. K. Lee, and W. Y. Yoon, *Acs Appl. Mater. Inter.* 5, 7058 (**2013**).
39. J. Shin, H. Jung, Y. Kim, and J. Kim, *J. Alloy Compd.* 589, 322 (**2014**).
40. M. Giorgetti, S. Mukerjee, S. Passerini, J. McBreen, and W. H. Smyrl, *Journal of the Electrochemical Society* 148, A768 (**2001**).
41. A. Q. Pan, H. B. Wu, L. Yu, T. Zhu, and X. W. Lou, *Acs Appl. Mater. Inter.* 4, 3874 (**2012**).
42. Y. Z. Zheng, H. Y. Ding, E. Uchaker, X. Tao, J. F. Chen, Q. F. Zhang, and G. Z. Cao, *J. Mater. Chem. A* 3, 1979 (**2015**).
43. Y. M. Liu, X. C. Zhou, and Y. L. Guo, *J. Power Sources* 184, 303 (**2008**).
44. S. Y. Chew, C. Q. Feng, S. H. Ng, J. Z. Wang, Z. P. Guo, and H. K. Liu, *J. Electrochem. Soc.* 154, A633 (**2007**).
45. A. Sakunthala, M. V. Reddy, S. Selvasekarapandian, B. V. R. Chowdari, and P. C. Selvin, *J. Phys. Chem. C* 114, 8099 (**2010**).
46. W. J. Wang, H. Y. Wang, S. Q. Liu, and J. H. Huang, *J. Solid State Electr.* 16, 2555 (**2012**).
47. X. Zhang and R. Frech, *Electrochim. Acta* 43, 861 (**1998**).
48. F. Haass, A. H. Adams, T. Buhrmester, G. Schimanke, M. Martin, and H. Fuess, *Phys. Chem. Phys.* 5, 4317 (**2003**).
49. G. A. Sawatzky and D. Post, *Phys. Rev. B* 20, 1546 (**1979**).
50. Y. Feng, Y. L. Li, and F. Hou, *J. Power Sources* 187, 224 (**2009**).
51. D. Liu, Y. Liu, B. B. Garcia, Q. Zhang, A. Pan, Y.-H. Jeong, and G. Cao, *J. Mater. Chem.* 19, 8789 (**2009**).
52. M. Park, X. C. Zhang, M. D. Chung, G. B. Less, and A. M. Sastry, *J. Power Sources* 195, 7904 (**2010**).
53. S. Sarkar, H. Banda, and S. Mitra, *Electrochim. Acta* 99, 242 (**2013**).
54. X. Xu, Y. Z. Luo, L. Q. Mai, Y. L. Zhao, Q. Y. An, L. Xu, F. Hu, L. Zhang, and Q. J. Zhang, *Npg. Asia. Mater.* 4 (**2012**).
55. J. Kawakita, Y. Katayama, T. Miura, and T. Kishi, *Solid State Ionics* 107, 145 (**1998**).
56. J. Kawakita, T. Miura, and T. Kishi, *J. Power Sources* 83, 79 (**1999**).
57. S. Huang, J. P. Tu, X. M. Jian, Y. Lu, S. J. Shi, X. Y. Zhao, T. Q. Wang, X. L. Wang, and C. D. Gu, *J. Power Sources* 245, 698 (**2014**).
58. S. Caes, J. C. Arrebola, N. Krins, P. Eloy, E. M. Gaigneaux, C. Henrist, R. Cloots, and B. Vertruyen, *J. Mater. Chem. A* 2, 5809 (**2014**).
59. M. Zhao, L. F. Jiao, H. T. Yuan, Y. Feng, and M. Zhang, *Solid State Ionics* 178, 387 (**2007**).
60. Z. J. Wu and Y. Zhou, *J. Power Sources* 199, 300 (**2012**).
61. S. Jouanneau, A. L. La Salle, A. Verbaere, M. Deschamps, S. Lascaud, and D. Guyomard, *J. Mater. Chem.* 13, 921 (**2003**).
62. S. Jouanneau, A. Verbaere, S. Lascaud, and D. Guyomard, *Solid State Ionics* 177, 311 (**2006**).
63. H. Y. Wang, K. L. Huang, Y. Ren, X. B. Huang, S. Q. Liu, and W. J. Wang, *J. Power Sources* 196, 9786 (**2011**).
64. Y. J. Kang, J. H. Kim, S. W. Lee, and Y. K. Sun, *Electrochimica. Acta* 50, 4784 (**2005**).
65. J. Fan and P. S. Fedkiw, *J. Power Sources* 72, 165 (**1998**).
66. N. H. Idris, M. M. Rahman, J. Z. Wang, Z. X. Chen, and H. K. Liu, *Compos. Sci. Technol.* 71, 343 (**2011**).
67. Y. K. Sun, J. M. Han, S. T. Myung, S. W. Lee, and K. Amine, *Electrochem. Commun.* 8, 821 (**2006**).

ARTICLE